DeCarbon 11 (2026) 100147

Contents lists available at ScienceDirect

DeCarbon

journal homepage: www.sciencedirect.com/journal/decarbon

Research Article

Property-control of self-assembled monolayer by employing hydroscopic polyethylene glycol for efficient and stable p-i-n perovskite solar cells

Jeewon Park[a,1], Faiza Shoukat[a,1], Wonjun Kim[a], Byongkyu Lee[a,c,*], Changduk Yang[a,b,c,**]

[a] School of Energy and Chemical Engineering, Ulsan National Institute of Science and Technology (UNIST), Ulsan, 44919, South Korea
[b] Graduate School of Carbon Neutrality, Ulsan National Institute of Science and Technology (UNIST), Ulsan, 44919, South Korea
[c] UNIST InnoCORE AI-Space Solar Initiative, Ulsan National Institute of Science and Technology (UNIST), Ulsan, 44919, South Korea

ARTICLE INFO

Keywords:
Hole transporting layer
Perovskite solar cell
Polyethylene glycol
Self-assembled monolayer

ABSTRACT

Recent great achievements of p-i-n perovskite solar cells (PSCs) have been mainly fueled by the development and advancement of carbazole-based self-assembled monolayers (SAMs) used as the hole-transport layers (HTLs). Driven by the success of polar, hydroscopic polyethylene glycol (PEG) application in the perovskite and buffer layers, herein we have assessed how the incorporation of PEG as ADDITIVE and BILAYER influences the SAM HTL in PSCs. When PEG is used as ADDITIVE, the photovoltaic performance of PSCs is reduced. While, PSCs processed by BILAYER exhibit high power conversion efficiencies (PCEs) of 24.75 % (lab-scale area: 0.039 cm^2) and 20.47 % (large area: 1 cm^2), attributed to the beneficial features such as better film/morphology formation and minimizing interfacial recombination losses/defect densities. Furthermore, we also demonstrate outstanding 73 % (after 1000 h, 25 °C, in ambient air) and 74 % (after 500 h, 85 °C, in inert) PCE retentions for the unencapsulated devices, accounting for stronger interaction between the PEG and perovskite layers. Our study paves a facile way of the polymeric materials' role played in the SAMs for improving the PCE and stability of PSCs through their surface modification.

1. Introduction

Recent advancements in perovskite solar cells (PSCs) have resulted in power conversion efficiencies (PCEs) exceeding 26 %, making them one of the most promising technologies for next-generation photovoltaic devices [1–4]. However, further enhancement of PSCs requires precise control over the interfaces between the perovskite active and charge-transport layers (CTLs: hole-transport layer (HTL) and electron-transport layer (ETL)). Despite the growing use of inorganic materials in these layers, their application is limited, which has led researchers to explore synthetic organic chemistry for tailoring material properties [5]. Among these, self-assembled monolayers (SAMs) based on organic materials have emerged as an attractive solution, offering advantages such as minimal material consumption, scalability, enhanced interfacial stability, and compatibility with environmentally friendly solvents [6,7]. In particular, carbazole-based SAMs (*e.g.*, [4-(3, 6-dimethyl-9*H*-carbazol-9-yl) butyl]phosphonic acid (Me-4PACz) and [4-(3,6-dimethoxy-9*H*-carbazol-9-yl) butyl] phosphonic acid (MeO-4PACz)) have been widely adopted as the HTLs in inverted PSCs, boosting the PCEs that rival or even surpass the n-i-p PSCs [8–12]. The SAM HTLs offer several advantages over traditional HTLs (*e.g.*, 2,2′,7,7′-tetrakis[N,N-di(4-methoxyphenyl)amino]-9,9′-spirobifluorene (spiro-OMeTAD) and polymer poly[bis(4-phenyl)(2,4,6-trimethylphenyl) amine] (PTAA): (i) the simple preparation process enables low-temperature treatments and full-solution fabrication, using significantly less material [13,14]; (ii) the ultrathin-film minimizes optical loss, enhancing the overall device performance [15]; (iii) the high-density ordered SAM structures facilitate efficient hole extraction by generating interfacial dipole moments [16,17]. Therefore, the delicate control of the SAM HTLs in terms of energy-level regulation, interface modification, defect passivation, and charge transportation is a crucial prerequisite toward achieving high PCEs of PSCs [17–22].

Polyethylene glycol (PEG) as a polar, hygroscopic polymer shows excellent thermodynamic property (softening at $\geq$ 60 °C), chemical stability, and low cost [23]. It has been directly incorporated into perovskite precursor solutions to enhance the stability of PSCs [24]. The

* Corresponding author.
** Corresponding author. School of Energy and Chemical Engineering, Ulsan National Institute of Science and Technology (UNIST), Ulsan, 44919, South Korea.
E-mail addresses: leebyongkyud@unist.ac.kr (B. Lee), yang@unist.ac.kr (C. Yang).
[1] These authors contributed equally to this work.

https://doi.org/10.1016/j.decarb.2026.100147
Received 7 November 2025; Received in revised form 28 December 2025; Accepted 27 January 2026
Available online 28 January 2026

C–O bonds (two lone electron pairs) in PEG backbone enable to interact with uncoordinated Pb^{2+} ions at the perovskite film surface by forming coordinate bonds, which can passivate the defects ultimately improve the device performances. Besides, many researchers reported the effective roles of PEG applications to improve both interfaces such as HTL/perovskite and perovskite/ETL) [25–27], providing positive impacts on reducing the defect density and interfacial recombination. These strategies can also allow the success of PSCs with enhanced PCE and stability.

Driven by the previous reports, we assume that PEG can serve as an effective functional interlayer in the SAM-employed PSCs (*e.g.*, optimizing wettability, promoting better film formation, and minimizing interfacial recombination losses). In this study, we investigated the roles of PEG in the MeO-4PACz SAM HTL of the PSCs. Fig. 1a schematically illustrates the proposed working mechanisms of PEG used as additive and bilayer within SAM HTL. Hereafter, we denoted as to 'CONTROL' fabricated by MeO-4PACz alone, 'ADDITIVE' with MeO-4PACz + PEG additive, and 'BILAYER' with MeO-4PACz + PEG layer, respectively. The ADDITIVE incorporation significantly deteriorates the device performance. However, the BILAYER device exhibited improved film/morphology formation and minimized interfacial recombination losses/defect densities, which enabled notable PCEs of 24.75 % (small-area device) and 20.47 % (1.0 cm^2 device), significantly higher than those of CONTROL ones. Besides, the stronger interaction observed between the hygroscopic PEG and perovskite contributed to excellent device stability of BILAYER-based unencapsulated devices, retaining over 73 % and 74 % of their initial PCEs after 1000 h, 25 °C, in ambient air and 500 h, 85 °C, in inert conditions, respectively.

2. Results and discussion

2.1. Interfacial electronic properties

We conducted ultraviolet photoelectron spectroscopy (UPS) of the films without and with PEG to its effect on the energy levels of MeO-4PACz SAM films. We note that PEG was added into SAM layer as an additive and deposited on the top of SAM layer as an interlayer, respectively, in which we used the optimal PEG concentration of 15 μL mL^{-1} in ethanol (see Experimental section for details). As shown in Fig. 1b, the highest occupied molecular orbital (HOMO)/lowest unoccupied molecular orbital (LUMO) levels were calculated as −5.48/−2.46, −5.28/−2.17, and −5.56/−2.59 eV for CONTROL, ADDITIVE, and BILAYER films, respectively. The BILAYER film shows a deeper HOMO level, being closer to that of the perovskite film, which can help reduce the hole transfer barrier and suppress non-radiative recombination at the interface. The hole injection barrier (HIB), denoted as ϕ_h, represents the energy difference between the HOMO band edge (at the interface) obtained from the secondary electron cut-off energy in the UPS spectrum and the work function (WF) of the substrate, as shown in Fig. 1c. The lower HIB value determined by the BILAYER film further confirmed its beneficial interface modification in terms of charge transport dynamics.

2.2. Photovoltaic performance

We fabricated p-i-n PSCs with a structure FTO/MeO-4PACz/perovskite/PDI/LiF/C60/BCP/Ag. The representative $J-V$ curves for respective PSCs are shown in Fig. 2a. The optimized CONTROL device exhibited a power conversion efficiency (PCE) of 22.65 % with open-circuit voltage (V_{OC}) of 1.15 eV, short-circuit current density (J_{SC}) of 24.43 mA/cm^2, and fill factor (FF) of 80.31 %. For the employed PEG cases, the ADDITIVE device yielded a lower PCE of 20.55 %, while the PCE of BILAYER device increased to 24.75 %, accompanied by enhancements in all the photovoltaic parameters. The detailed photovoltaic parameters are summarized in Table 1. The superior PCE in BILAYER device should be partially correlated with the suitable tuning of energy level alignment above.

Fig. 2b presents the statistical distribution of PCEs extracted from the fabricated devices as a function of different HTLs. Moreover, inspired by the excellent performance brought by BILAYER configuration HTL, we extended our research to PSCs with a large active area (1.0 cm^2) as shown in Fig. 2c. Similar to small-size cell tests, the BILAYER device

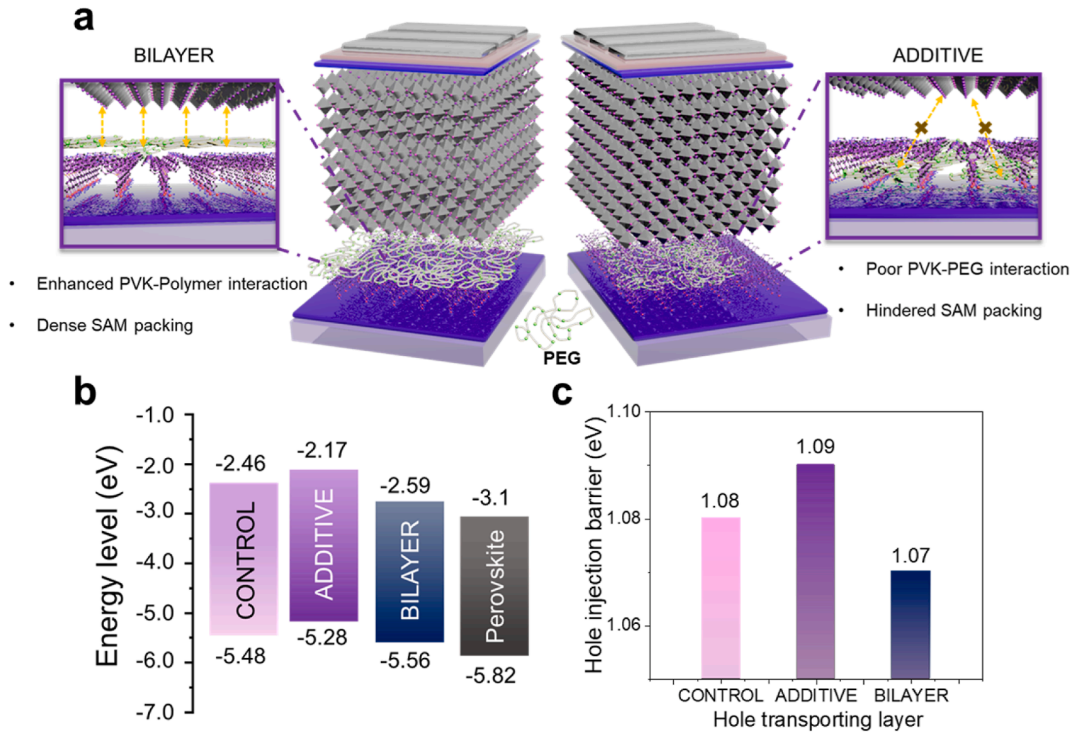

Fig. 1. (a) Conceptual illustration elucidating the underlying mechanism of ADDITIVE and BILAYER (b) Energy level alignments for a range of hole transport layers (HTLs). (c) Comparison of hole injection barriers across different HTLs.

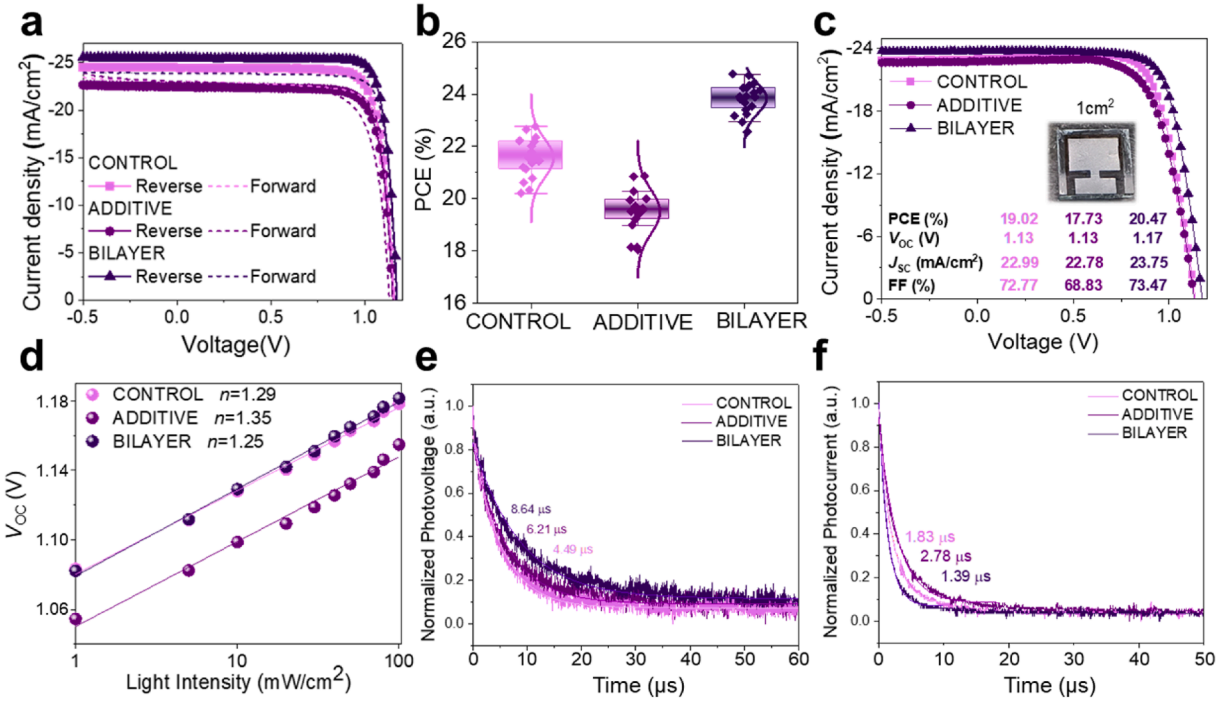

Fig. 2. (a) Current-voltage (*J*–*V*) characteristics. (b) Statistical distribution of power conversion efficiencies (PCEs) for 20 individual devices. (c) *J*-*V* characteristics of a device with an active area of 1.0 cm^2. (d) Light intensity dependence of the open-circuit voltage (V_{OC}). (e) Transient photovoltage (TPV) and (f) Transient photocurrent (TPC) measurements of the Control-, Additive-, and Bilayer-based devices.

Table 1
Device parameters of CONTROL, ADDITIVE, and BILAYER devices.

Device	V_{OC}[1] [V]	J_{SC}[1] [mA/cm^2]	FF[1] [%]	PCE[1] [%]
CONTROL	1.15 (1.14 ± 0.009)	24.43 (23.01 ± 0.80)	80.31 (79.79 ± 0.61)	22.65 (21.15 ± 0.76)
ADDITIVE	1.14 (1.16 ± 0.008)	22.47 (22.13 ± 0.56)	79.79 (78.79 ± 0.89)	20.55 (20.02 ± 0.66)
BILAYER	1.16 (1.16 ± 0.007)	25.48 (24.97 ± 0.69)	83.10 (82.10 ± 0.82)	24.75 (23.87 ± 0.68)

[1] Average device parameters are shown with an error range of one standard deviation (20evices were tested for statistics).

yielded far better PCE of 20.47 % compared to the others (CONTROL (19.02 %) and ADDITIVE (17.73 %)).

Further, to determine the charge recombination status in device, the light intensity dependence of V_{OC} of devices was measured. The BILAYER device had a lower slope (n) value of 1.25 kT/q than those of the others (CONTROL (1.29 kT/q) and ADDITIVE (1.35 kT/q), as seen from Fig. 2d, where k, T, and q are the Boltzmann constant, Kelvin temperature, and charge, respectively. The lowest n value for the bilayer indicates that it has the least Shockley-Read Hall (SRH) recombination at the perovskite interface [6]. Therefore, from this result, the trap-assisted recombination was significantly reduced in BILAYER device, which can be recognized as a defect-passivation effect at the BILAYER/perovskite interface, resulting in increasing of device performance.

Transient photovoltage/photocurrent (TPV/TPC) measurements were carried out to investigate the charge-carrier dynamics in the devices under open-circuit and short-circuit conditions, respectively. As shown in Fig. 2e, the photovoltage decay times obtained from TPV were 8.64 μs for the CONTROL device, 6.21 μs for the ADDITIVE-based device, and 4.49 μs for the BILAYER-based device. The TPC results (Fig. 2f) show that the photocurrent decay time was 1.83 μs for the CONTROL device, decreased to 1.39 μs for the BILAYER device, but increased to 2.78 μs for the ADDITIVE device. These results confirm the reduced recombination and improved charge extraction capability in the case of BILAYER. Conversely, the BILAYER configuration effectively minimizes recombination losses, which contributes to its superior photovoltaic performance.

2.3. Morphology and charge transport properties

We characterized the microscopic morphology of the HTLs films via atomic force microscopy (AFM), scanning electron microscopy (SEM), and X-ray diffraction (XRD) measurements, respectively. As shown in Fig. 3a, the BILAYER film has a smoother surface with a root-mean-square (RMS) roughness of 30.6 nm than that of CONTROL (37.9 nm) and ADDITIVE (35.1 nm) films, which is convenient for good contact between SAM layer and top perovskite film [16]. Besides, as verified by the top-view scanning electron microscope (SEM) images in Fig. 3b, the perovskite film on BILAYER substrate has smoother surface and larger grains than those of the CONTROL and ADDITIVE cases. It is evident that larger grains help to reduce the density of grain boundaries, which are places for non-radiative recombination, while the CONTROL and ADDITIVE films exhibit rough surfaces, uneven grain sizes, and indistinct grain boundaries, which can promote the defect formation [28,29].

Fig. 3c presents the X-ray diffraction (XRD) patterns, in a closer look around (100) diffraction peak regions (see Fig. 3d), an additional peak at 11.45° appears in the BILAYER, likely due to PEG forming hydrogen bonds and coordinating with Pb^{2+} ions, which creates a unique intermediate phase that influences perovskite crystallization. We quantified the 11.45° feature by peak fitting and found that its normalized integrated intensity is significant only for the BILAYER, suggesting a minor PEG–Pb^{2+} coordination-induced intermediate/adduct-like phase at the HTL/perovskite interface (Fig. S1 and Table S1). We also found that in the comparison, the BILAYER exhibits smaller full width at half

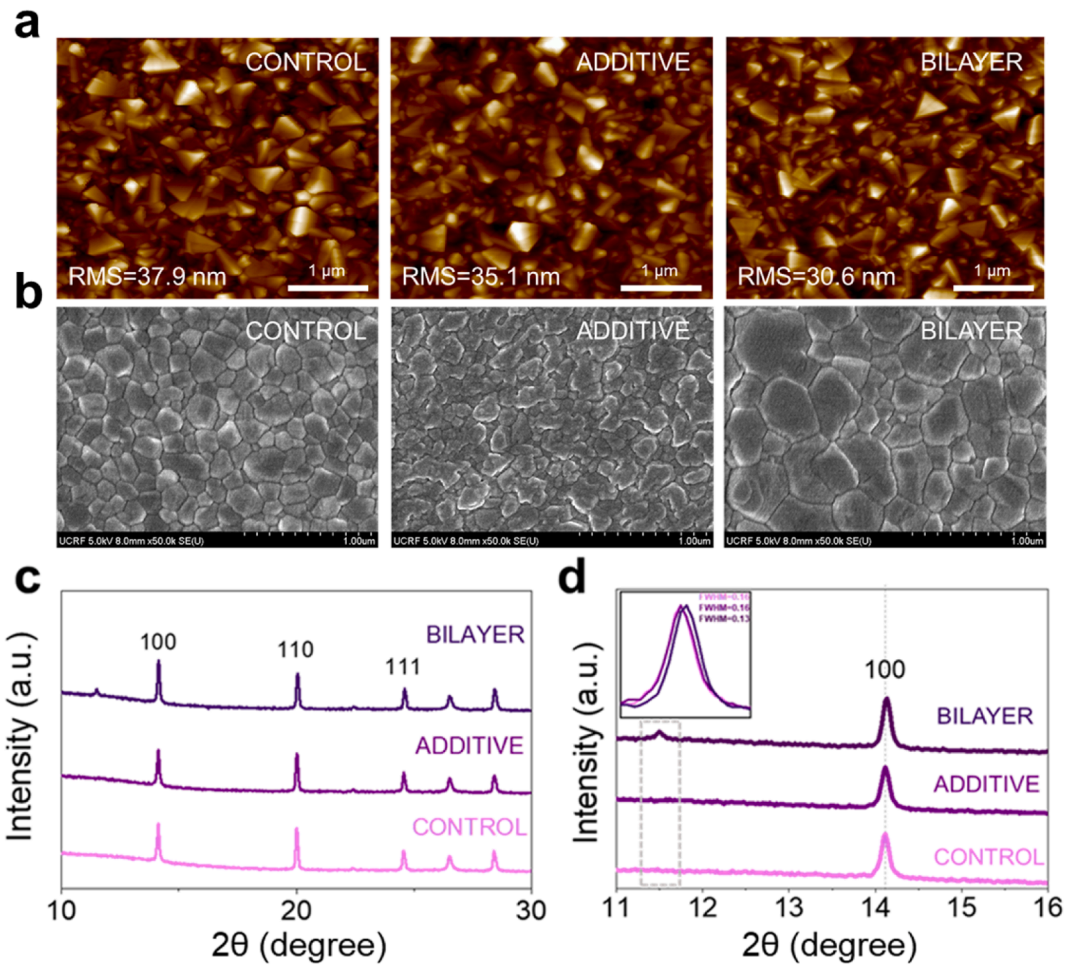

Fig. 3. (a) Atomic force microscopy (AFM) images of various hole transport layers (HTLs) on FTO substrate. (b) Scanning electron microscopy (SEM) images of perovskite films deposited on different substrates. (c) X-ray diffraction (XRD) patterns of perovskite films with three HTLs. (d) Fitting analysis of the (100) peak in XRD data with inset showing the Full Width at Half Maximum (FWHM) values of the (100) diffraction peak for perovskite films.

maximum (FWHM) (0.13) of the (100) diffraction peak with slightly intensified intensity, indicating a better perovskite-film quality with larger grains and fewer grain boundaries (GBs) [30]. The detailed XRD parameters such as crystal size and *d*-spacing are summarized in Table S2.

To evaluate defect densities in perovskite films, space-charge-limited-current (SCLC) measurements were performed on hole-only devices with an FTO/HTL/perovskite/MoO_3/Ag structure. As shown in Fig. 4a and Table S3, the cross points of ohmic region and trap-filling region indicate the trap-filled limit voltage (V_{TFL}), which are determined to be 0.40 V, 0.45 V and 0.26 V for CONTROL, ADDITIVE and BILAYER devices, respectively. The lower trap density within the BILAYER device implies enhanced hole transport properties, thus increasing V_{OC} and FF as observed earlier [6]. The trap-state density (N_t) is positively correlated with the V_{TFL}. The N_t values was calculated as 8.3×10^{14}, 9.3×10^{14}, and 5.4×10^{14} cm^{-3} for devices based on CONTROL, ADDITIVE and BILAYER, respectively. The decreased N_t in BILAYER can be originated from the defect-passivation effect on the bottom interface of the perovskite.

For a thorough understanding of the charge carrier dynamics at the buried interface, we performed photoluminescence (PL) and Time-resolved photoluminescence (TRPL) measurements, as depicted in Fig. 4b and Fig. S2. In addition to significantly enhanced PL intensity, the BILAYER film exhibited a longer average carrier lifetime (τ_{avg}) of 1425.58 ns compared to the others (ADDITIVE (710.04 ns) and the CONTROL (526.10 ns)). These results are attributed to the reduced the non-radiative recombination pathway as a result of better defect-passivation effects of BILAYER [17,31]. Table S4 presents the detailed results calculated from the biexponential fitting of TRPL curves.

To investigate the interaction between perovskite and MeO-4PACz SAM with and without PEG, the X-ray photoelectron spectroscopy (XPS) was carried out. As shown in Fig. 4c and d, the CONTROL film showed the characteristic peaks of O 1s and C 1s within MeO-4PACz unit at binding energy of 530.59 eV and 284.02 eV, respectively. Upon the presence of PEG, these peaks were shifted toward higher binding energy: The ADDITIVE film displayed the coexistence of small shifted original O 1s and C 1s peaks and the additional peaks in high binding energy regions, corresponding to the interaction between MeO-4PACz and PEG. On the other hand, the single peaks large-shifted to the high energy (533.04 eV (O 1s) and 286.79 eV (C 1s)) were observed in BILAYER film, indicating a stronger interaction between MeO-4PACz and PEG.

As illustrated in Fig. 4e and f, the contrasting effects of PEG in the ADDITIVE and BILAYER HTL configurations arise from its interaction with the MeO-4PACz SAM at the ITO interface. In the ADDITIVE case, PEG co-adsorption disrupts SAM formation/packing, leading to a poorly defined hole-selective contact and increased interfacial trap-assisted non-radiative recombination. By contrast, in the BILAYER configuration, the MeO-4PACz SAM remains intact, while the PEG layer acts as a secondary interfacial modifier that promotes favorable perovskite nucleation/morphology and passivates interfacial defects, enabling efficient hole extraction and improved device performance.

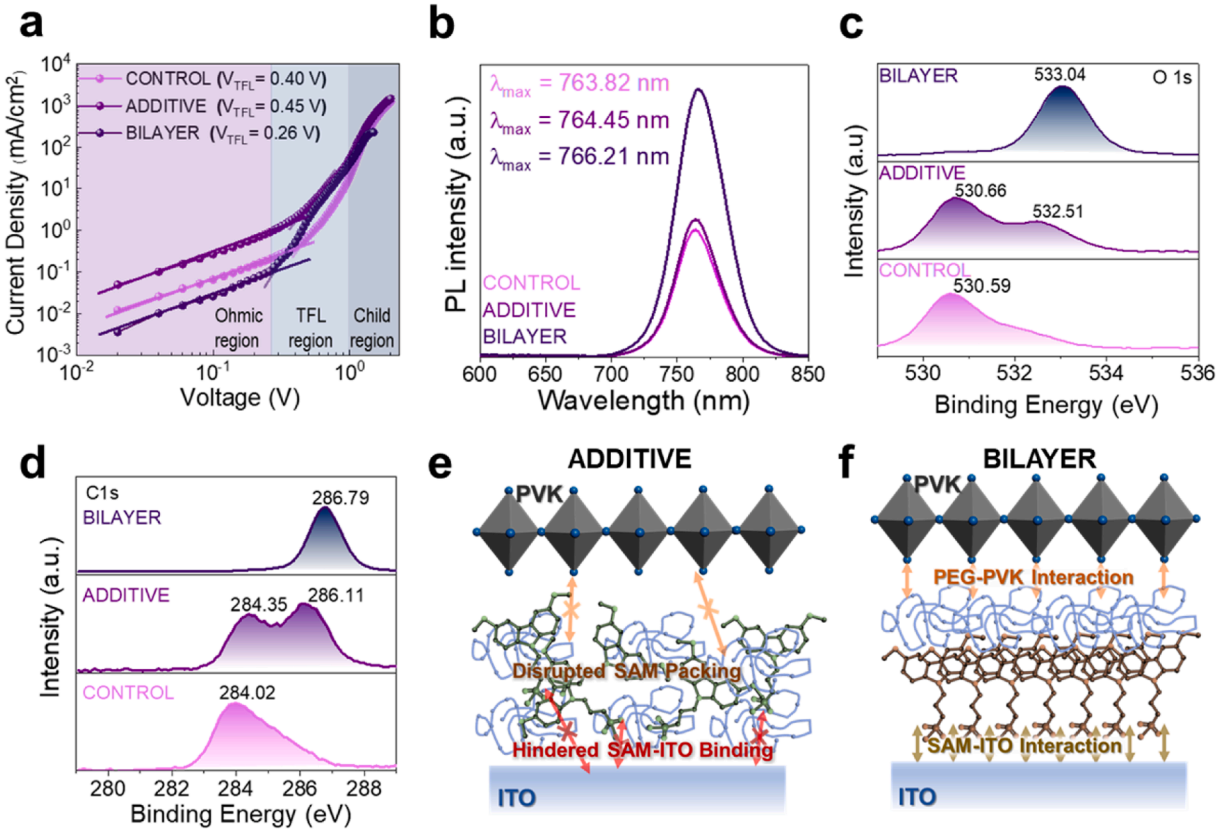

Fig. 4. (a) Space-charge-limited current (SCLC) characterization of hole-only devices with the architecture FTO/HTL/Perovskite/Spiro-OMeTAD/MoO_3/Ag. (b) Photoluminescence (PL) spectra of the perovskite films deposited on three different HTLs. X-ray photoelectron spectroscopy (XPS) spectra of (c) O 1s and (d) C 1s for the corresponding samples. Schematic illustration of the working mechanisms of devices employing (e) ADDITIVE and (f) BILAYER HTLs.

2.4. Device stability

The stability of unencapsulated devices was evaluated under ambient air (25 °C, 30 % relative humidity (RH)) and thermal (85 °C in an inert) conditions, respectively. As shown in Fig. 5a, the BILAYER device retained 73 % of its initial PCE after 1000 h in ambient air conditions, outperforming CONTROL (61 %) and ADDITIVE (63 %) devices. Similarly, under the thermal stress, the BILAYER device again showed much better PCE retention (over 74 %) 500 h compared to the others tested under the same conditions (Fig. 5b). The improved stability results of the BILAYER devices can originate from improved film morphology and reduced defect density induced by the stronger interaction between the PEG and perovskite [32].

3. Conclusions

In summary, the roles of polar, hygroscopic PEG played in the MeO-4PACz SAM HTL of the PSCs (as ADDITIVE and BILAYER, respectively) were properly investigated. The ADDITIVE structure had somewhat negative impacts on the frontier energy levels and the relation to PSC device performance. In a sharp contrast, the BILAYER structure enabled superior PCEs of 24.75 % (lab-scale area) and 20.47 % (large area), which was significantly higher than that observed for CONTROL due to multiple benefits such as better film/morphology formation and minimizing interfacial recombination losses/defect densities. Moreover, the BILAYER-based unencapsulated devices retained 73 % and 74 % of their initial PCEs after 1000 h, at room temperature in ambient air and 500 h

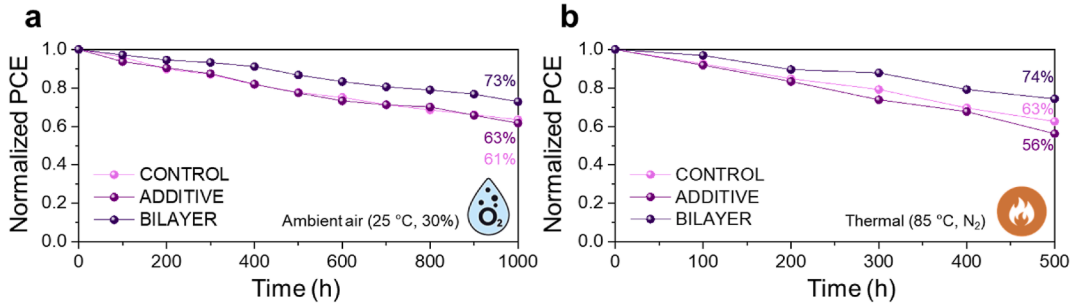

Fig. 5. Stability test of Control, Additive-based, and Bilayer-based unencapsulated devices (a) under ambient air conditions with relative humidity (RH) of 30 ± 5 %. (b) at 85 °C in a nitrogen-filled glove box.

at 85 °C in inert conditions, respectively, while CONTROL ones maintained only 61 % and 56 % in the same conditions. The enhanced stability of BILAYER devices should be also correlated with reduced density and improved morphology derived by the stronger interaction between the hygroscopic PEG and perovskite. Our studies offer a simple, easy way to stimulatingly improve the performance and stability of PSCs.

4. Experimental section

4.1. Materials

All chemicals employed in the experiment were purchased from Sigma-Aldrich and TCI Chemicals. Acetone (99.5 %, Samchun Chemicals), 2-propanol (IPA, 99.5 %, Samchun Chemicals), anhydrous ethanol (Sigma-Aldrich), anhydrous dimethylsulfoxide (DMSO, Sigma-Aldrich), anhydrous dimethylformamide (DMF, Sigma-Aldrich), anhydrous ethyl acetate (Sigma-Aldrich), were procured and used directly for substrate cleaning, solvent preparation, and antisolvent dropping without further purification. MeO-4PACz (TCI), formamidinium iodide (FAI, Greatcell Solar), cesium iodide (CsI, ultradry, 99.999 % Alfa Aesar), lead iodide (PbI_2, TCI), piperazinium diiodide (PDI, Greatcell Solar), C60 (99.99 %, OSM), and Ag (99.9999 %, iTASCO) were acquired and utilized without additional purification procedures.

4.2. Device fabrication

The FTO substrates were cleaned using ultrasonic treatment in deionized water, acetone, and isopropanol, followed by overnight drying in an oven. Subsequently, the substrates underwent UV–ozone treatment for 20 min. A MeO-4PACz solution (0.5 mg mL^{-1} in ethanol) was spin-coated onto the FTO substrate at 3000 rpm for 30 s, followed by annealing at 100 °C for 10 min. PEG was dissolved in ethanol to prepare a uniform solution with a concentration of 0.1 mg mL^{-1}. For the ADDITIVE approach, a 10:1 ratio of SAM to PEG was used for mixing. In the BILAYER approach, the PEG layer (0.1 mg mL^{-1}) was spin-coated at 3000 rpm, followed by thermal annealing at 100 °C for 10 min.

$Cs_{0.185}FA_{0.815}Pb(I_{0.875}Br_{0.125})_3$ perovskite precursor solution was prepared by using DMF:DMSO (4:1). Briefly, perovskite films were deposited via a solvent engineering method by spin coating a precursor solution in two steps at 3500 rpm for 30 s and then at 6500 rpm for 5 s. Anhydrous ethyl acetate (200 μL) was dripped at the center of the substrate during the second step. After spin-coating, transfer it to a hot plate at 100 °C for annealing for 30 min. Transfer the above-mentioned substrate into a vacuum chamber and thermally evaporate LiF (1 nm), C_{60} (20 nm), BCP (8 nm), and Ag (120 nm) sequentially.

4.3. Device characterization

Photocurrent density-voltage *J–V* curves were recorded using a Keithley 2400 source under illumination of a solar simulator (SX1100, Enlitech) with an intensity of AM 1.5G 100 mW cm^{-2} calibrated by a Newport 91150-KG5 reference solar cell. EQE measurements were conducted by using a solar-cell spectral-response measurement system (QE-R3011, Enlitech). AFM images of the films were taken by Dimension ICON (Bruker). photoluminescence (PL) measurements were conducted using ELCT-3010 PL mode (Enlitech). X-ray Photoelectron Spectroscopy (XPS) was performed using K-alpha (ThermoFisher).

CRediT authorship contribution statement

Jeewon Park: Writing – original draft, Investigation, Conceptualization. **Faiza Shoukat:** Writing – original draft, Validation, Formal analysis, Data curation, Conceptualization. **Wonjun Kim:** Validation, Data curation. **Byongkyu Lee:** Writing – review & editing, Visualization. **Changduk Yang:** Writing – review & editing, Validation, Supervision, Resources, Funding acquisition, Conceptualization.

Data availability

Data will be made available on request.

Declaration of competing interest

The authors declare that they have no known competing financial interests or personal relationships that could have appeared to influence the work reported in this paper.

The author Dr. Changduk Yang is an Associate Editor for DeCarbon and was not involved in the editorial review or the decision to publish this article.

Acknowledgement

This work was supported by the InnoCORE program of the Ministry of Science and ICT (1.260007.01) and the Nano & Material Technology Development Program through the National Research Foundation of Korea (NRF) funded by Ministry of Science and ICT (RS-2025-25442266). We thank UNIST Office of Research Facilities and Training (ResFacT) for support of using the equipment.

Appendix A. Supplementary data

Supplementary data to this article can be found online at https://doi.org/10.1016/j.decarb.2026.100147.

References

[1] J. Park, J. Kim, H.-S. Yun, M.J. Paik, E. Noh, H.J. Mun, M.G. Kim, T.J. Shin, S. I. Seok, Controlled growth of perovskite layers with volatile alkylammonium chlorides, Nature 616 (2023) 724–731.
[2] Z. Xiong, Q. Zhang, K. Cai, H. Zhou, Q. Song, Z. Han, S. Kang, Y. Li, Q. Jiang, X. Zhang, J. You, Homogenized chlorine distribution for >27% power conversion efficiency in perovskite solar cells, Science 390 (2025) 638–642.
[3] Z. Wang, C. Gong, C. Zhang, C. Zhao, T.-S. Su, H. Li, H. Zhang, Recent advances in interfacial engineering for high-efficiency perovskite photovoltaics, DeCarbon 8 (2025) 100107.
[4] J. Park, S. Kim, W. Kim, Z. Sun, B. Lee, C. Yang, Stepwise volatilization induced by nature-sourced volatile solid additives improving the efficiency and stability of perovskite solar cells, Energy Environ. Sci. 18 (2025) 6260–6272.
[5] G. Qu, S. Cai, Y. Qiao, D. Wang, S. Gong, D. Khan, Y. Wang, K. Jiang, Q. Chen, L. Zhang, Y.-G. Wang, X. Chen, A.K.-Y. Jen, Z.-X. Xu, Conjugated linker-boosted self-assembled monolayer molecule for inverted perovskite solar cells, Joule 8 (2024) 1–12.
[6] M.-H. Yu, X. Liu, H.-W. Yu, S.-F. Kao, C.-H. Chen, Y.-C. Tseng, I.-C. Ni, B.-H. Lin, Y. Wang, C.-C. Chueh, Impact of self-assembled monolayer structural design on perovskite phase regulation, hole-selective contact, and energy loss in inverted perovskite solar cells, Nano Energy 132 (2024) 110405.
[7] J. Zeng, L. Bi, Y. Cheng, B. Xu, A.K.-Y. Jen, Self-assembled monolayer enabling improved buried interfaces in blade-coated perovskite solar cells for high efficiency and stability, Nano Res. Energy 1 (2022) e9120004.
[8] A. Farag, T. Feeney, I.M. Hossain, F. Schackmar, P. Fassl, K. Küster, R. Bäuerle, M. A. Ruiz-Preciado, M. Hentschel, D.B. Ritzer, A. Diercks, Y. Li, B.A. Nejand, F. Laufer, R. Singh, U. Starke, U.W. Paetzold, Evaporated self-assembled monolayer hole transport layers: lossless interfaces in p-i-n perovskite solar cells, Adv. Energy Mater. 13 (2023) 2203982.
[9] T. Wu, S. Mariotti, P. Ji, L.K. Ono, T. Guo, I.-N. Rabehi, S. Yuan, J. Zhang, C. Ding, Z. Guo, Y. Qi, Self-assembled monolayer hole-selective contact for up-scalable and cost-effective inverted perovskite solar cells, Adv. Funct. Mater. 34 (2024) 2316500.
[10] Z. Yi, X. Li, Y. Xiong, G. Shen, W. Zhang, Y. Huang, Q. Jiang, X.R. Ng, Y. Luo, J. Zheng, W.L. Leong, F. Fu, T. Bu, J. Yang, Self-assembled monolayers in inverted perovskite solar cells and their tandem photovoltaics application, Interdiscip. Mater. 3 (2024) 203–244.
[11] S. Liu, K. Wang, W. Sun, J. Liang, Z. Li, J. Song, S. Wang, C. Chen, H. Zhu, A donor–acceptor-type hole-selective self-assembled monolayer for inverted perovskite solar cells with improved efficiency and stability, Adv. Energy Mater. 13 (2023) 2301706.
[12] F.H. Isikgor, S. Zhumagali, L.V.T. Merino, M. De Bastiani, I. McCulloch, S. De Wolf, Molecular engineering of contact interfaces for high-performance perovskite solar cells, Nat. Rev. Mater. 8 (2023) 89–108.
[13] Y. Zhang, Y. Liu, Z. Zhao, T. Kong, W. Chen, W. Liu, P. Gao, D. Bi, Improving buried interface contact for inverted perovskite solar cells via dual modification strategy, Adv. Funct. Mater. 34 (2024) 2417575.

[14] W. Li, E. Martínez-Ferrero, E. Palomares, Self-assembled molecules as selective contacts for efficient and stable perovskite solar cells, Mater. Chem. Front. 8 (2024) 681–699.
[15] C. Li, Y. Chen, Z. Zhang, C. Liu, F. Guo, W. Ahmad, P. Gao, Pros and cons of hole-selective self-assembled monolayers in inverted PSCs and TSCs: extensive case studies and data analysis, Energy Environ. Sci. 17 (2024) 6157–6203.
[16] I. Levine, A. Al-Ashouri, A. Musiienko, H. Hempel, A. Magomedov, A. Drevilkauskaite, V. Getautis, D. Menzel, K. Hinrichs, T. Unold, S. Albrecht, T. Dittrich, Charge transfer rates and electron trapping at buried interfaces of perovskite solar cells, Joule 5 (2021) 2915–2933.
[17] X. Deng, F. Qi, F. Li, S. Wu, F.R. Lin, Z. Zhang, Z. Guan, Z. Yang, C.-S. Lee, A.K.-Y. Jen, Co-assembled monolayers as hole-selective contact for high-performance inverted perovskite solar cells with optimized recombination loss and long-term stability, Angew. Chem. Int. Ed. 61 (2022) e202203088.
[18] E. Li, E. Bi, Y. Wu, W. Zhang, L. Li, H. Chen, L. Han, H. Tian, W.-H. Zhu, Synergistic coassembly of highly wettable and uniform hole-extraction monolayers for scaling-up perovskite solar cells, Adv. Funct. Mater. 30 (2020) 1909509.
[19] H. Zhou, W. Wang, Y. Duan, R. Sun, Y. Li, Z. Xie, D. Xu, M. Wu, Y. Wang, H. Li, Q. Fan, Y. Peng, Y. Yao, C. Liao, Q. Peng, S. Liu, Z. Liu, Glycol monomethyl ether-substituted carbazolyl hole-transporting material for stable inverted perovskite solar cells with efficiency of 25.52, Angew. Chem. Int. Ed. 63 (2024) e202403068.
[20] A. Al-Ashouri, M. Marcnskas, E. Kasparavicus, T. Malinauskas, A. Palmstrom, V. Getautis, S. Albrecht, M.D. McGehee, A. Magomedov, Wettability improvement of a carbazole-based hole-selective monolayer for reproducible perovskite solar cells, ACS Energy Lett. 8 (2023) 898–900.
[21] K. Hossain, A. Kulkarni, U. Bothra, B. Klingebiel, T. Kirchartz, M. Saliba, D. Kabra, Resolving the hydrophobicity of the Me-4PACz hole transport layer for inverted perovskite solar cells with efficiency >20%, ACS Energy Lett. 8 (2023) 3860–3867.
[22] L. Li, Y. Wang, X. Wang, R. Lin, X. Luo, Z. Liu, K. Zhou, S. Xiong, Q. Bao, G. Chen, Y. Tian, Y. Deng, K. Xiao, J. Wu, M.I. Saidaminov, H. Lin, C.-Q. Ma, Z. Zhao, Y. Wu, L. Zhang, H. Tan, Flexible all-perovskite tandem solar cells approaching 25% efficiency with molecule-bridged hole-selective contact, Nat. Energy 7 (2022) 708–717.
[23] F. Deng, X. Sun, X. Lv, Y. Li, S. Li, Y.-Z. Zheng, X. Tao, All room-temperature processing efficient planar carbon-based perovskite solar cells, J. Power Sources 489 (2021) 229345.
[24] W. Xu, T. Zhu, H. Wu, L. Liu, X. Gong, Poly(ethylene glycol) diacrylate as the passivation layer for high-performance perovskite solar cells, ACS Appl. Mater. Interfaces 12 (2020) 45045–45055.
[25] Y. Wang, J. Ye, J. Song, J. Cao, P. Zhou, X. Xu, Q. Zhou, G. Li, Y. Tu, L. Chu, Y. Zang, X. Yin, Y. Jin, Z. Su, L. Hu, Z. Li, W. Yan, Synchronous modulation of hole-selective self-assembled monolayer and buried interface for inverted perovskite solar cells, Cell Rep. Phys. Sci. 5 (2024) 101992.
[26] S. Park, D. Kim, S. Kim, H. Kim, K. Kim, H.J. Son, Effect of polyethylene glycol incorporation in SnO_2 electron transport layer for high-efficiency perovskite solar cells, Sol. Energy 231 (2022) 119–126.
[27] D.H. Sin, S.B. Jo, S.G. Lee, H. Ko, M. Kim, H. Lee, K. Cho, Enhancing the durability and carrier selectivity of perovskite solar cells using a blend interlayer, ACS Appl. Mater. Interfaces 9 (2017) 18103–18112.
[28] M. Pitaro, J.S. Alonso, L. Di Mario, D.G. Romero, K. Tran, T. Zaharia, M. B. Johansson, E.M.J. Johansson, M.A. Loi, A carbazole-based self-assembled monolayer as the hole transport layer for efficient and stable $Cs_{0.25}FA_{0.75}Sn_{0.5}Pb_{0.5}I_3$ solar cells, J. Mater. Chem. A 11 (2023) 11755–11766.
[29] C. Zhang, X. Wan, J. Zang, Q. Liu, Y. Fei, Z. Yu, Polymer-modified $CsPbI_2Br$ films for all-inorganic planar perovskite solar cells with improved performance, Surf. Interfaces 22 (2021) 100809.
[30] Y. Guo, L. Huang, C. Wang, J. Huang, S. Liu, X. Liu, J. Zhang, Z. Hu, Y. Zhu, Efficient inverted perovskite solar cells with a low-temperature processed NiOx/SAM hole transport layer, J. Mater. Chem. C 12 (2024) 1507–1515.
[31] Y. Zhao, Y. Liu, Z. Ren, Y. Li, Y. Zhang, F.-C. Kong, T. Liu, X. Shi, Y. Dou, L. Wang, F. Wang, X. Guo, Y. Cao, W. Wang, P.C.Y. Chow, S. Chen, Enhanced interface adhesion with a polymeric hole transporter enabling high-performance air-processed perovskite solar cells, Energy Environ. Sci. 17 (2024) 4699–4710.
[32] P. Deng, W. Dai, Y. Gou, W. Zhang, Z. Xiao, S. He, X. Xie, K. Zhang, J. Li, X. Wang, L. Lin, Improving thermal stability of high-efficiency methylammonium-free perovskite solar cells via chloride additive engineering, ACS Appl. Mater. Interfaces 16 (2024) 29338–29346.